Chemistry and Materials

The Center for Science Innovation

Research Article

Chem. Mater. 4 (3) 2025, 117-129

Synthesis of Hematite Using Different Additives and The Fabrication of Hematite/SiO_2 Composite

Shirly Harissyah Alfiani, Qori'atun Ni'mah Salsabila, Reinardo Ramawijaya Widakusuma, Agus Purwanto*, Rifqi Almusawi Rafsanjani, Habib Muhammad Zapar, Bagaskoro Pranata Ardhi

Cipta Mikro Material, Jl. Komp. Puspitek, Pengasinan, Gn. Sindur, Bogor, West Java 16340, Indonesia

*Corresponding author: agus.purwanto@cipta-mikro-material.com

Received
02 June 2025

Received in revised form
15 August 2025

Accepted
08 September 2025

DOI
https://doi.org/10.56425/cma.v4i3.107

Abstract

Hematite (α-Fe_2O_3) is a widely studied iron oxide due to its broad functional versatility in catalysis, sensing, and environmental applications. However, controlling its morphology and crystallinity remains a challenge, which limits its performance in composite materials. This study investigates the role of sodium hydroxide and citric acid as additives to identify optimal hematite characteristics on the fabrication of hematite/SiO_2 composite via the sol-gel method. Sodium hydroxide serves as a source of hydroxide ions, accelerating nucleation and acting as a precipitating agent, while citric acid chelates Fe^{3+} ions and caps growing nuclei, which enhances crystallinity and suppresses particle agglomeration. As a result, hematite$_{CA}$ exhibited brownish-purple appearance and higher crystallinity, whereas hematite$_{SH}$ showed larger and more agglomerated particles. Integrating silica into hematite$_{CA}$ produced wine-red hematite/SiO_2 composites and porous-like surface morphology. These findings demonstrate that additive selection is a critical parameter in synthesizing hematite microstructure and enhancing its compatibility with silica, thereby enabling the development of composites for advanced applications.

Keywords: hematite, additives, silica

1. Introduction

Nanoparticles (NPs) are at the forefront of nanotechnology development, offering size-dependent properties that make them indispensable across diverse scientific and industrial sectors [1–3]. Among them, metal oxide NPs have garnered considerable attention due to their wide-ranging applications in catalysis, sensing, energy storage, biomedical engineering, and magnetic technologies [4–6]. Iron oxide NPs, in particular, are notable for their low toxicity [3,7], thermodynamic stability [7], anticorrosion properties [4], and favorable optical characteristics [8]. Iron oxides occur in several polymorphic forms, including magnetite (Fe_3O_4), akaganeite (β-Fe_2O_3), maghemite (γ-Fe_2O_3), and hematite (α-Fe_2O_3) [4,9].

Hematite (α-Fe_2O_3) is the most thermodynamically stable iron oxide phase under ambient atmospheric conditions [5,10]. Its abundance, low cost, chemical durability, and n-type semiconducting behavior (band gap ≈2.1 eV) make it attractive for applications ranging from pigments [11], gas sensors [12], catalysis [13], lithium-ion battery [14], and magnetic materials [3]. However, the performance of hematite materials is highly dependent by its crystallinity, particle size, and morphology [15]. Over the past few decades, much effort has been made in the design of various hematite materials with a desired structure and morphology, such as tubes [16], urchinlike [17], belts [18], flakes [18], rods [19], spindles [20], flowers [21], rings [22], platelets [23], cubes [23], ellipsoids [23], peanut [23], bipyramid [23], spheres [23], fibers [24], hollow fibers [25], and complex hierarchical structures constructed with nanoscale building blocks and ordered mesoporous hematite. These varied morphologies expose distinct crystallographic facets, each characterized by unique atomic configurations that directly influence the material's surface reactivity, electronic behavior, and interactions with the surrounding environment [3]. Consequently, the precise control over particle size and morphology is essential.

One effective strategy to achieve such control is through the use of additives during the synthesis process [26]. For instance, Bai *et al.* [28] reported that varying citric acid concentrations during synthesis produced distinct morphologies, from flower-like clusters in its absence to nanosheets (≈250 nm) at low concentrations, and self-assembled nanorods (≈80 nm diameter) at higher concentrations. Similarly, Liu *et al.* [29] also reported that the amount of sodium hydroxide introduced into the mixture directly influenced the acidic degree of the solution, thereby controlling the morphology and particle size distribution.

Additives such as inorganic anions (e.g., sulfate, phosphate, hydroxide) and organic chelating agents (e.g., citric acid) can modulate nucleation and growth kinetics, thereby influencing particle size distribution, shape evolution, and crystallinity [27]. Sodium hydroxide serves as a source of hydroxide ions that accelerate nucleation and act as a precipitating agent, whereas citric acid chelates Fe^{3+} ions and caps growing nuclei, which not only enhances crystallinity but also suppresses particle agglomeration [26–28]. The selection of these two additives was intended to assess which synthesis condition would yield hematite with more favorable characteristics, particularly smaller particle size or less agglomeration.

Nevertheless, hematite still encounters challenges related to colloidal instability and particle aggregation, impairing their functional performance. An effective strategy to address these limitations is immobilizing hematite onto high surface area supports, particularly porous materials [2,30]. Among these, Silica has attracted significant research interest due to its advantageous properties, including high surface area, tunable pores, high adsorption capacity, and excellent stability [31]. These features improve particle dispersion, prevent aggregation, and enhance access to catalytic sites [32]. Porous silica has been widely employed as a catalyst support across various catalyst, including hematite [31]. Previous studies show that adding silica to hematite-based catalysts significantly boosts their performance by increasing surface area, improving reactant access, and enhancing structural stability [31]. For instance, Lubis *et al* [33] reported that integrating silica into hematite enhanced its photocatalytic efficiency, with the hematite/SiO_2 composite achieving acid black 1 (AB1) degradation efficiency of 85.86%, compared to 50.89% for pure hematite. The increased degradation efficiency could come from the higher adsorption ability of AB1 on the surface of hematite/SiO_2 composite (65.97%) than hematite (36.71%).

Hematite/SiO_2 composites can be synthesized using methods such as the sol-gel process with silica templating. Silica acts as a structural guide, allowing control over morphology and creating surface porosity that increases surface area and functional properties [34,35]. Delahaye *et al.* [36] successfully reported the synthesis of mesoporous hematite/SiO_2 using a templating approach, where hematite particles were confined within the ordered pore channels of silica, resulting in a homogeneous dispersion with an average crystallite size of 15 nm.

In this study, hematite was synthesized using two different additives, citric acid and sodium hydroxide. The hematite sample that exhibited the highest crystallinity and smallest crystallite size was selected for incorporation with purified silica to fabricate a hematite/SiO_2 composite. This synthesized composite has considerable potential for a wide range of applications, including catalyst.

2. Materials and Method

2.1 Materials

The chemicals used in this study were iron (III) chloride ($FeCl_3$, ≥98%, Merck), citric acid monohydrate ($C_6H_8O_7·H_2O$, ≥99%, Merck), ethanol (C_2H_5OH, ≥98%, Merck), sodium hydroxide (NaOH, ≥98%, Merck), distilled water, and silica, which was obtained from the purification of geothermal waste.

2.2 Silica purification from geothermal waste

The geothermal byproduct obtained from PT Geo Dipa Energi was first sieved to ensure uniform particle size. The material was then washed with deionized water under continuous stirring to remove surface impurities. After washing, it was dried at 100 °C for 24 h and sieved again through a 150 µm mesh. The pre-treated powder was dissolved in a 1.5 M sodium hydroxide solution and heated to 90 °C under vigorous stirring to form a sodium silicate solution. The solution was filtered to remove insoluble residues, and the filtrate was titrated with 10% HCl until a neutral pH was reached, resulting in the formation of white silica gel. The gel was aged for 24 h and oven-dried at 125 °C. The solid was then ground into a fine powder and calcined at 500 °C.

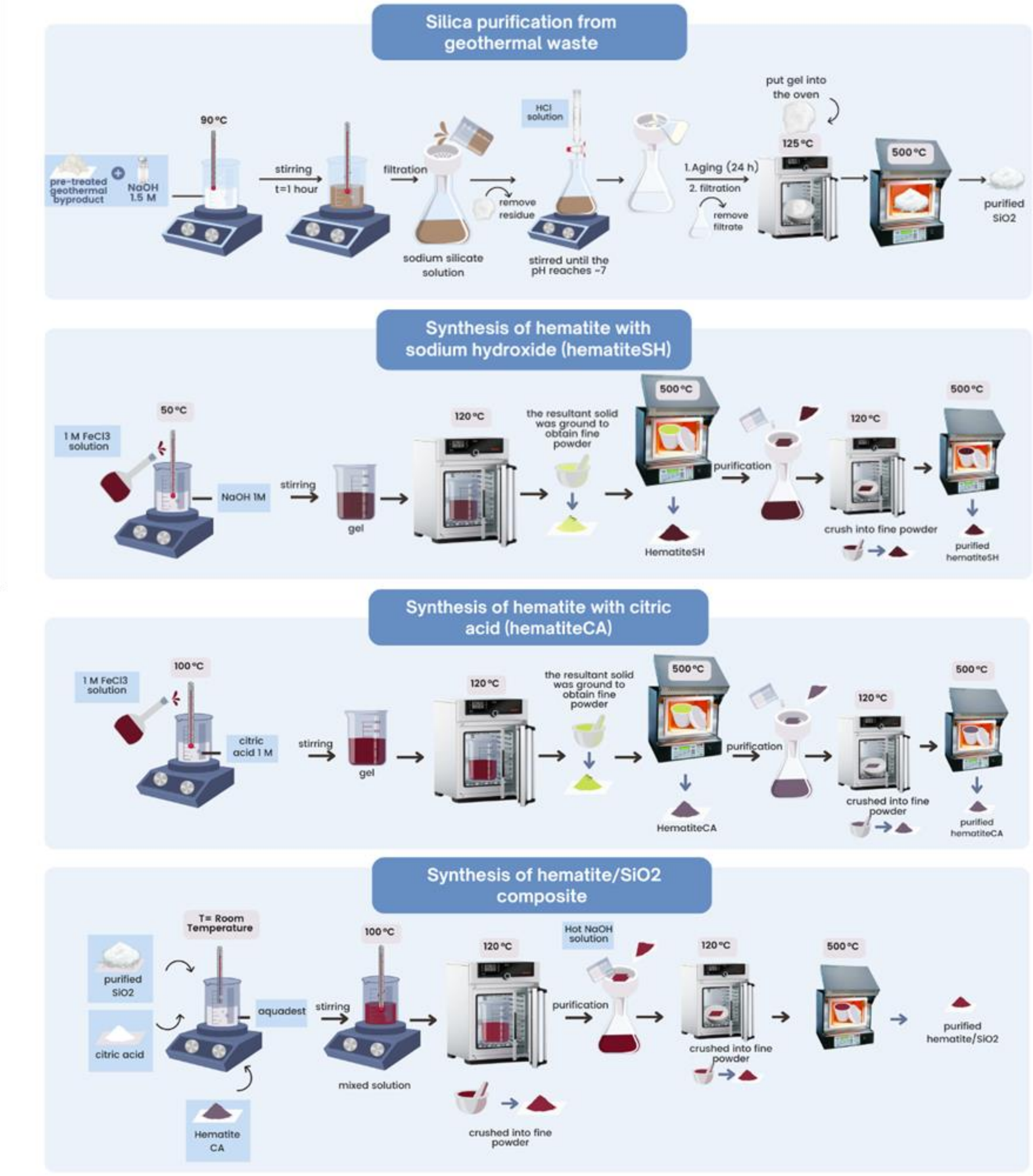

Figure 1. Schematic illustration of silica purification and the synthesis processes of hematite$_{CA}$, hematite$_{SH}$, and hematite/SiO_2 composite.

2.3 Synthesis of hematite

Hematite NPs were synthesized through sol–gel methods, employing sodium hydroxide and citric acid as additives**.** In the sodium hydroxide-assisted route, a 1 M $FeCl_3$ solution was slowly introduced into the sodium hydroxide solution (1M) under constant stirring at 50 °C until a homogeneous gel formed. The gel was oven-dried at 120 °C, ground into a fine powder, and subsequently calcined at 500 °C for 6 h. The final product from this pathway was named hematite$_{SH}$. In the citric-acid-assisted route, a 1 M $FeCl_3$ solution was gradually introduced into a 1 M citric acid solution under continuous stirring, and the mixture was then heated to 100 °C to promote gelation. The gel was oven-dried at 120 °C, ground into a powder, and calcined under identical conditions (500 °C, 6 h). The final product from this pathway was named as hematite$_{CA}$. For both pathways, post-synthesis purification involved dispersing the calcined powder in a 100 mL ethanol–water mixture (60:40 v/v), followed by vacuum filtration, oven-drying at 120 °C, and calcined at 500 °C for 6 h.

2.4 Synthesis of hematite/SiO_2 composite

Hematite/SiO_2 composite was synthesized using hematite from citric acid-assisted route (hematite$_{CA}$). The hematite$_{CA}$ powder, citric acid, and purified SiO_2 were dissolved in 50 mL of distilled water with a total molar ratio of 1:1:3. The mixture was stirred at 100 °C until gelation occurred, followed by oven-drying at 120 °C, and pulverization. The resulting powder was washed with hot NaOH solution, filtered, and the precipitates were oven-dried at 120 °C. The resulting was then finely ground and calcined at 500 °C for 6 h.

2.5 Characterization

The chemical composition, surface morphology, elemental distribution, and crystalline phases of the samples were analyzed using X-ray fluorescence (XRF, Malvern Panalytical Epsilon 4), scanning electron microscopy-energy dispersive X-ray spectroscopy (SEM-EDS, Thermo Fisher Prisma), and X-ray diffraction (XRD, Malvern Panalytical Aeris, Co Kα, λ = 0.179 nm, 2θ = 5°–100°). The SEM images were processed with ImageJ software, while the diffraction patterns were analyzed with PANalytical Highscore Plus software and matched to the international centre for diffraction data (ICDD) or crystallography open database (COD) databases. The average crystallite size of the samples was calculated using the Debye-Scherrer equation:

$$D = \frac{K\lambda}{\beta \cos \theta} \quad (1)$$

where D is the crystallite size, K is the Scherrer constant (0.9), λ is the wavelength of the X-rays used (0.179 nm), β is the full width at half maximum ($FWHM$, radians), and θ is the Bragg angle (radians) [37].

3. Results and Discussion

3.1 Silica purification from geothermal waste

The sol–gel method was employed for silica purification, encompassing sequential stages of hydrolysis, condensation, aging, drying, and calcination [38,39]. This stage aims to prepare silica (SiO_2) as a template for synthesizing hematite/SiO_2 composites [35]. During the purification process, sodium hydroxide dissociates, yielding Na^+ and OH^- ions. The hydroxide ions act as nucleophiles and undergo nucleophilic interaction with silicon (Si) atoms in the silica (SiO_2) framework. This interaction disrupts the Si–O bonds through the high electronegativity of oxygen and leads to the formation of SiO_2OH^- species, which subsequently release hydrogen ions (H^+) [40]. The cleavage of additional Si–O bonds lead to the formation of silicate anions (SiO_3^{2-}). These anions react with Na^+ ions to produce sodium silicate (Na_2SiO_3), while the remaining OH^- ions combine with H^+ to generate water (H_2O) [41]. The mechanism of sodium silicate formation is illustrated in Fig 2.

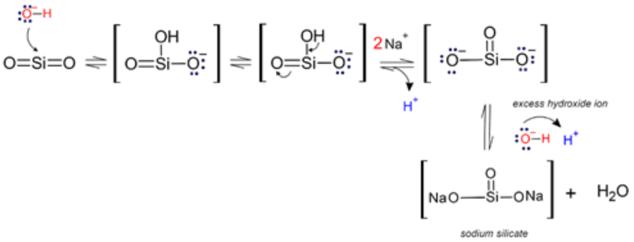

Figure 2. Mechanism reaction of sodium silicate formation.

Moreover, heating and stirring during the process could accelerate the reaction rate and enhance the interaction between solute and solvent [42]. The overall reaction between silica and sodium hydroxide can be represented by the following equation [43]:

$$SiO_{2(s)} + 2NaOH_{(aq)} \rightarrow Na_2SiO_{3(aq)} + H_2O_{(l)} \quad (2)$$

The obtained sodium silicate (Na_2SiO_3) solution was then titrated with hydrochloric acid (HCl) until the solution reached a stable neutral pH (≈7). The introduction of HCl initiates the protonation, forming Na^+ ions and silicate ions (SiO_3^{2-}). The Na^+ ions then react with Cl^- ions to form NaCl, thereby reducing the solution's pH [40]. This acidification triggers the hydrolysis of silicate ions (SiO_3^{2-}) to form $Si(OH)_4$, which subsequently undergoes condensation to generate siloxane (Si–O–Si) linkages (Fig 3) [41].

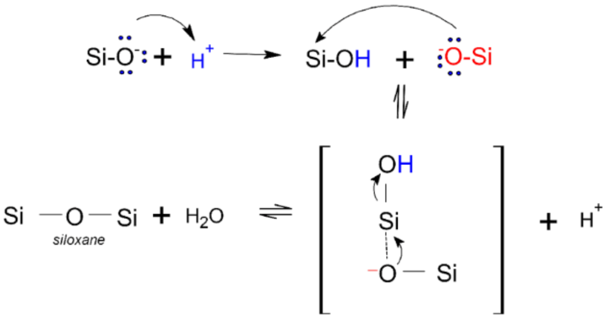

Figure 3. Reaction Mechanism of Siloxane Bond Formation.

As these linkages grow, they assemble into colloidal particles (sol phase) that progressively interconnect to form a continuous three-dimensional network. Upon reaching the gelation threshold, the viscosity of the system increases sharply, resulting in the formation of silica gel [40]. Precise pH control to neutral conditions is essential during this process. If the pH shifts into the more acidic range, the precipitated silica may redissolve, reducing its structural stability and leading to undesirable outcomes in the final product [42]. The overall reaction can be represented as follows [44]:

$$Na_2SiO_{3(aq)} + 2HCl_{(aq)} \rightarrow SiO_{2(s)} + 2NaCl_{(aq)} + H_2O_{(l)} \quad (3)$$

Table 1. XRF results of silica before and after purification.

Compound	Concentration (Before Purification)	Concentration (After Purification)
SiO_2	92.407 %	97.655 %
P_2O_5	1.256 %	1.124 %
Cl	4.658 %	0.705 %
K_2O	0.708 %	-
CaO	0.573 %	0.278 %
CuO	0.016%	0.004 %
ZnO	0.047 %	0.019 %
As_2O_3	0.246 %	0.003 %
Sb_2O_3	0.068 %	0.015 %
TeO_2	0.005 %	-
PbO	0.015 %	0.005 %

XRF analysis results (Table 1) reveal a notable increase in silica (SiO_2) purity from 92.40% to 97.65% following purification, confirming the effectiveness of the applied sol–gel–based protocol. Phosphorus pentoxide (P_2O_5) remained the second most abundant constituent, decreasing only slightly from 1.256% to 1.124%. The persistence of P_2O_5 impurities has also been reported by Novita *et al.* [41], who observed 3.49% P_2O_5 in purified SiO_2 derived from palm kernel shell ash. This indicates that further purification is required, employing specific reagents that can remove phosphorus oxide impurities. Cai *et al.* [45] suggests that treatment with 1% oxalic acid ($H_2C_2O_4$) could reduce P_2O_5 impurity by up to 77.7%.

The significant reduction in chloride concentration from 4.65% to 0.70% indicates that chloride salts are highly soluble and were effectively removed during the acid-washing process. This removal was further facilitated by the reaction between Na^+ and Cl^- ions during titration. Potassium oxide (K_2O) and tellurium dioxide (TeO_2) were completely removed, falling below the detection limit.

Heavy metal oxides, including CuO and ZnO, showed substantial decreases attributed to their dissolution during the purification process. Other oxides, such as As_2O_3 and Sb_2O_3, also diminished significantly, likely due to vaporization during the calcination step at 500 °C.

The X-ray diffraction (XRD) pattern of the purified silica (Fig 4) exhibits a broad hump and low-intensity peak, showing a characteristic of amorphous materials. This broad peak appears from the absence of long-range atomic order that usually seen in the crystalline phases [46]. In XRD pattern, the amorphous silica typically displays the broad hump between $2\theta = 15°$ and $35°$ [47]. From the XRD characterization, the purified silica in this research showed a peak at $2\theta = 21.728°$ (COD-4124063) [48–51]. This result aligns with the previous research conducted by Utama *et al* [47].

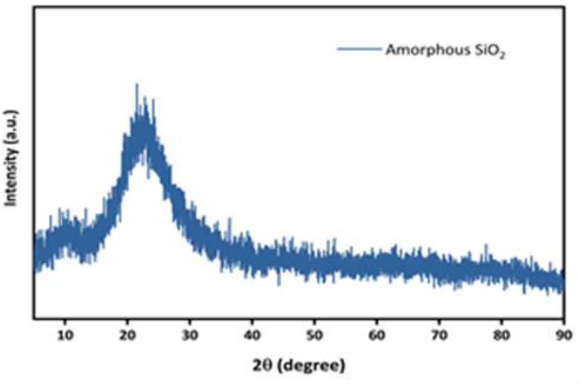

Figure 4. XRD pattern of purified silica.

3.2. Synthesis of hematite

In the sodium hydroxide-assisted route, ferric chloride ($FeCl_3$) was employed as the source of Fe^{3+} ions, while sodium hydroxide (NaOH) served as the precipitating agent [52]. Sodium hydroxide (NaOH) is a strong alkali that readily dissociates in aqueous media, instantaneously supplying hydroxide ions (OH^-) into the reaction environment [53]. The introduction of these OH^- ions elevate the solution pH, creating strongly basic conditions that favor the rapid hydrolysis and precipitation of ferric ions (Fe^{3+}) [52].

At the initial stage, Fe^{3+} ions react with hydroxide ions (OH^-), forming ferric hydroxide $Fe(OH)_3$ as a brown gel-like precipitate. Concurrently, sodium cations (Na^+) combine with chloride anions (Cl^-) to produce soluble sodium chloride (NaCl) as a reaction byproduct (Equation 4) [52]. The precipitate is then oven-dried at 120 °C to promote dehydration and structural rearrangement of $Fe(OH)_3$ into goethite (α-FeOOH) through the elimination of lattice water (Equation 5). This transformation is visually confirmed by the change in product appearance, from brown to yellowish green. The overall reaction for synthesizing hematite$_{SH}$ can be represented as follows:

$$FeCl_{3(aq)} + 3NaOH_{(aq)} \rightarrow Fe(OH)_{3(s)} + 3NaCl_{(aq)} \quad (4)$$

$$Fe(OH)_{3(s)} \rightarrow FeOOH_{(s)} + H_2O_{(l)} \quad (5)$$

$$2FeOOH_{(s)} \rightarrow Fe_2O_{3(s)} + H_2O_{(l)} \quad (6)$$

In the citric acid-assisted route, Fe^{3+} ions released from $FeCl_3$ interact with the carboxyl (-COOH) functional groups of citric acid. These groups undergo deprotonation to yield negatively charged carboxylate ($–COO^-$) groups, whose lone electron pairs can be donated into the vacant orbitals of Fe^{3+}, forming stable coordinate covalent bonds [54]. This interaction leads to the formation of ferric–citrate complexes [55,56]. The structure of the complex can vary based on the reaction conditions used. One key factor that influences the formation of this complex is the molar ratio of Fe^{3+} to citrate ions [57]. Below are the possible complex structures that may form:

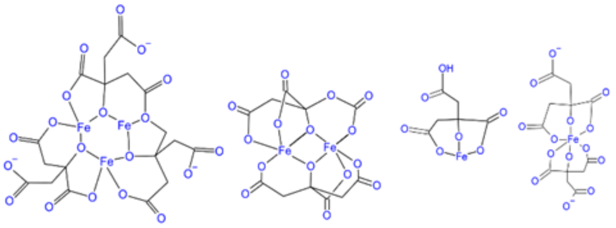

Figure 5. The possible ferric-citrate structures that may formed.

The formed ferric–citrate complex undergoes gradual hydrolysis, releasing Fe^{3+} ions in a controlled manner. These ions subsequently participate in a condensation reaction, leading to the formation of M–O–M (metal–oxygen–metal) linkages. At this stage, citric acid ligands control particle growth through steric hindrance and electrostatic stabilization, allowing condensation to proceed gradually. As the process continues, the particles connect to form a three-dimensional gel network, with citric acid acting as a bridge between them [58]. At this stage, a brown gel is formed and subsequently oven-dried at 120 °C for two hours. Upon completion of the drying and grinding steps, the resulting powder appears as yellowish green powder, that is closely similar to the solid obtained from previous synthesis (hematite$_{SH}$).

In the final stage, the yellowish-green powders obtained from the sodium hydroxide and citric acid-assisted synthesis routes underwent calcination at 500 °C, yielding hematite$_{SH}$ and hematite$_{CA}$, respectively [59,60]. After calcination, noticeable color changes were observed. Hematite$_{SH}$ exhibits a dark brown color, appearing almost black, whereas hematite$_{CA}$ exhibits a lighter brown with a hint of purple. The coloration of hematite is strongly influenced by particle size. A transition from reddish-brown to purple or black signifies an increase in particle size [61].

The XRF characterization results for hematite$_{SH}$ and hematite$_{CA}$ are presented in Table 2. The data indicate that α-Fe_2O_3 is the dominant phase in both materials, with concentrations of 93.219% for hematite$_{SH}$ and 96.731% for hematite$_{CA}$. This confirms that the synthesis process successfully produced hematite, with hematite$_{CA}$ exhibiting higher purity than hematite$_{SH}$.

Table 2. XRF results of hematite$_{SH}$ and hematite$_{CA}$.

Compound	hematite$_{SH}$	hematite$_{CA}$
α-Fe_2O_3	93.219 %	96.731%
Cl	0.22 %	0.596 %
P_2O_5	1.231 %	1.264%
SiO_2	4.972 %	0.112 %

In addition, minor impurities were detected. Both samples contained small amounts of chlorine (Cl), likely originating from residual precursor salts used during synthesis. Hematite$_{CA}$ showed a slightly higher Cl content (0.596%) than hematite$_{SH}$ (0.22%). Phosphorus pentoxide (P_2O_5) was also present in similar concentrations for both samples (1.23-1.26%), which may be attributed to trace contaminants from reagents or the reaction environment. The presence of SiO_2 and P_2O_5 impurities in the synthesized hematite has also been reported by Fatmaliana *et al.* [62]. To reduce P_2O_5 impurities, additional washing steps that are more effective against phosphates should be considered.

The EDS results (Table 3) confirm the successful formation of hematite in both samples, corroborating the XRF findings. Hematite$_{CA}$ shows higher Fe content (69.4 wt%) compared to hematite$_{SH}$ (43.0 wt%), indicating higher purity in hematite$_{CA}$. Chlorine (Cl) was also detected at low concentration in hematite$_{CA}$ (0.7 wt%) but undetectable in hematite$_{SH}$, likely due to its very low concentration. The detected Na content (22.0 wt%, 24.3 at%) in hematite$_{SH}$ may originate from the formation of byproduct that occurs during the synthesis process.

Table 3. Elemental composition of hematite$_{SH}$ and hematite$_{CA}$ based on EDS spectra.

Elements	Line	Hematite$_{CA}$		Hematite$_{SH}$	
		At%	Wt%	At%	Wt%
C	K	11.3 %	4.4 %	6.9 %	3.3 %
O	K	49.5 %	25.5 %	47.8 %	30.1 %
Cl	K	0.6 %	0.7 %	-	-
Fe	K	38.6%	69.4 %	19.6 %	43.0 %
Si	K	-	-	1.4 %	1.6 %
Na	K	-	-	24.3 %	22.0 %

The SEM images reveal distinct morphological differences between hematite$_{SH}$ (Fig 6A) and hematite$_{CA}$ (Fig 6B), highlighting the influence of additives on particle characteristics. Hematite$_{SH}$ (Fig 6A) displays a dense and highly agglomerated morphology composed of irregularly shaped particles tightly clustered together, exhibiting rough and uneven surfaces with sizes ranging from 4.25 to 30.32 μm (average: 13.69 μm). The irregular shapes and severe agglomeration observed in hematite$_{SH}$ may result from some factors, including the concentration ratio of $FeCl_3$ and sodium hydroxide precursors. Rinda *et al.* [2] reported that the higher concentration of sodium hydroxide (3:1 ratio) resulted in homogenous particles with a small average size and spherical morphology.

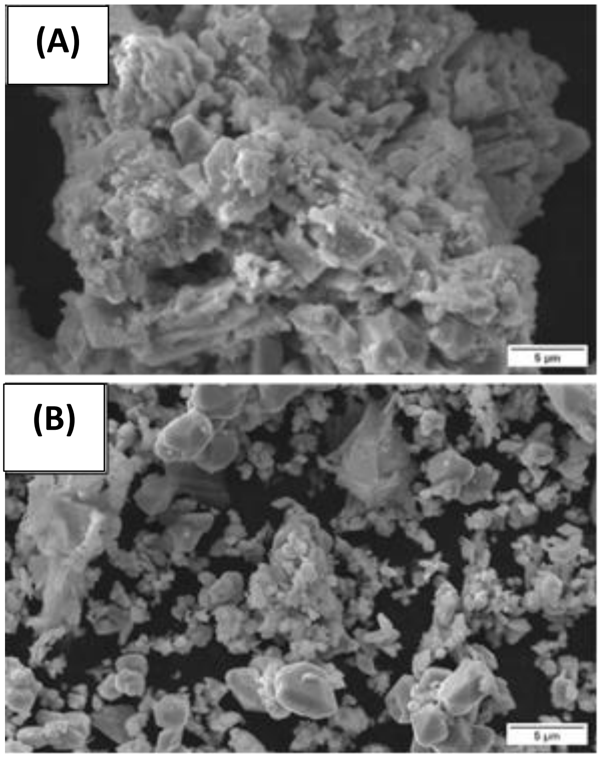

Figure 6. SEM images of hematite$_{SH}$ (A) and (B) hematite$_{CA}$.

In contrast, hematite$_{CA}$ (Fig 6B) displays smaller particle sizes (0.30–5.69 µm; average 1.77 µm) and a lower degree of agglomeration compared to hematite$_{SH}$. The particles of hematite$_{CA}$ predominantly exhibit a hexaferrite morphology. This observation is consistent with the findings of Marjeghal *et al*. [63], who reported that synthesized hematite using citric acid by sol-gel method tends to form hexaferrite structures.

The agglomeration in hematite$_{CA}$ can be attributed to several factors, including the concentration ratio of citric acid and $FeCl_3$ precursor, which showed a similar issue to that of hematite$_{SH}$. Marjeghal *et al.* [63] reported that low concentrations ratio of citric acid to ferric nitrate (0.5:1 and 1:1) led to the formation of bigger, more agglomerated particles, while higher ratios (2:1 and 4:1) led to more disperse and smaller particles. Moreover, the agglomeration may also result from high calcination temperatures and the presence of weak intermolecular forces (eg. hydrogen bonds or van der Waals forces) on hematite surface [63–65].

The analysis of XRD patterns from both samples revealed distinct peaks characteristic of hematite (Fig 7). In the hematite$_{SH}$ sample (blue line), diffraction peaks were observed at 2θ = 27.98° (0 1 2), 38.56° (1 0 4), 41.48° (1 1 0), 47.69° (1 1 3), 57.99° (0 2 4), 63.57° (1 1 6), 67.70° (1 2 2), 73.85° (0 1 8), 75.80° (2 1 4), and 85.86° (1 0 1 0), which matched the reference database (ICDD No. 01-079-1741). Additional low-intensity peaks at 2θ = 24.09°, 27.81°, and 39.63° were also detected in hematite$_{SH}$, corresponding to sodium phosphate (Na_3PO_4) impurities that might form during the sodium hydroxide-assisted synthesis. The presence of these peaks reinforces the EDS findings, which revealed a substantial Na content in hematite$_{SH}$. The formation of sodium phosphate (Na_3PO_4) could be attributed to various factors, including synthesis conditions and precursor purity [66].

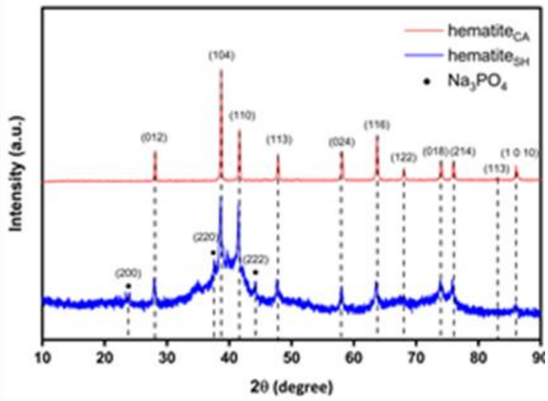

Figure 7. XRD patterns of hematite$_{SH}$ and hematite$_{CA}$.

Compared to hematite$_{CA}$, the hematite$_{SH}$ diffraction peaks are broader and of lower intensity, indicating lower crystallinity and a larger crystallite size than hematite$_{CA}$. Debye-Scherrer calculations of all observed peaks show that hematite$_{SH}$ has an average crystallite size of 64.93 nm compared to 13.58 nm for hematite$_{CA}$. This interpretation is consistent with the SEM results, where hematite$_{SH}$ exhibits irregular morphologies with severe agglomeration, potentially hindering ordered crystal growth. Furthermore, the reduced crystallinity of hematite$_{SH}$ may also be influenced by the presence of sodium phosphate (Na_3PO_4) impurities detected in its XRD pattern and EDS results, introducing amorphous or poorly crystalline phases [67].

The hematite$_{CA}$ diffraction peaks (red line) appear at slightly different angles than those of hematite$_{SH}$, with peaks observed at 2θ = 28.11° (0 1 2), 38.70° (1 0 4), 41.62° (1 1 0), 47.83° (1 1 3), 50.99° (2 0 2), 58.13° (0 2 4), and 63.71° (1 1 6), also identified using the same database (ICDD No. 01-079-1741). The diffraction peak shift of hematite$_{CA}$ is attributed to the presence of organic anions from citrate, which can shift the position toward higher 2θ values and distort the lattice parameters during hematite formation [68]. The peaks indexed as (1 0 4) and (1 1 0) exhibited the highest intensity and sharpest peaks, indicating the high degree of crystallinity [56].

Based on XRF, EDS, SEM, and XRD results, it is evident that hematite$_{SH}$ is less promising due to their low purity and crystallinity, larger particles size, and highly agglomerated particles. The poor quality of hematite$_{SH}$ is likely due to the concentration ratios of NaOH and $FeCl_3$ precursor, leading to uncontrolled precipitation and promotes the formation of byproducts [2]. In contrast, the use of citric acid in synthesizing hematite$_{CA}$ proved highly effective in producing a pure hematite phase with smaller particle size, reduced agglomeration, and enhanced crystallinity. Citric acid likely acts as a chelating and capping agent, controlling Fe^{3+} ion hydrolysis and growth kinetics, thereby enabling the formation of more homogeneous and structurally ordered particles [26–28]. These characteristics make hematite$_{CA}$ an optimal precursor for hematite/SiO_2 composite fabrication.

3.3. Synthesis of hematite/SiO_2 composite

Hematite$_{CA}$ was used to synthesize a hematite/SiO_2 composite through the addition of silica. During synthesis, citric acid acts as a chelating agent that facilitates the formation of complexes [56].

The XRF characterization results of hematite/SiO_2 are presented in Table 4. The analysis reveals that the composite remains predominantly composed of hematite (α-Fe_2O_3). However, the hematite content in hematite/SiO_2 composite (87.86 wt%) is markedly lower than the initial material (hematite$_{CA}$, see Table 2). This reduction in the wt% of hematite primarily attributed to the high SiO_2 content (7.763 wt%) and other impurities, such as P_2O_5, CaO, and Cl, which likely originated from the purified silica (Table 1) and hematite$_{CA}$ (Table 2). These results highlight the necessity for further purification to enhance phase purity and minimize residual contaminants.

Table 4. XRF result of hematite/SiO_2 composite.

Compounds	hematite/SiO_2 composite (wt%)
α-Fe_2O_3	87.863 %
SiO_2	7.763 %
P_2O_5	1.216 %
CaO	1.763 %

Figure 8 illustrates the formation of agglomerated, irregularly shaped particles of hematite/SiO_2 composite, with particle sizes ranging from 50 nm to 22 µm and an average of 15.25 µm. This observation aligns with the findings of Hassan *et al*. [55], who reported that incorporating SiO_2 into hematite powder during synthesis frequently yields clumped, irregular particle morphologies. Moreover, the presence of pore-like structure was also observed on the surface of hematite/SiO_2 composite.

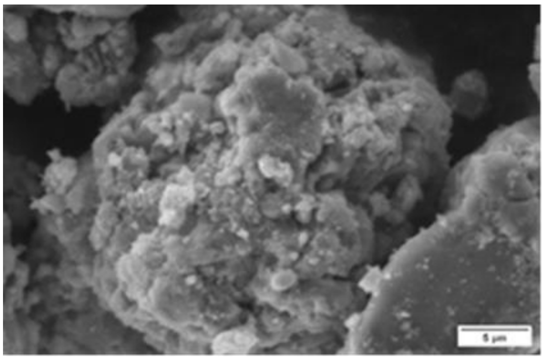

Figure 8. SEM images hematite/SiO_2 composite.

This result is similar to the porous hematite synthesized by Gritli *et al.* [9]. However, to confirm the porosity of the hematite particles, further analysis using BET or TEM is necessary. The presence of porosity in hematite samples has the potential to enhance reaction efficiency by providing a larger surface area during interactions [69].

The EDS analysis (Table 5) revealed that the hematite/SiO_2 composite mainly consisted of iron (Fe) and oxygen (O), with weight percentages of 49.4 wt% and 27.7 wt%, respectively. This composition confirms the successful formation of hematite (α-Fe_2O_3) as the primary phase. Other detected elements such as Si, Na, Mg, and Al, may likely originate from environmental contaminants during synthesis, while Ca was presumed to originate from the purified silica (Table 1).

Table 5. Elemental composition of hematite/SiO_2 composite based on the EDS Spectra.

Elements	Line	hematite/SiO_2	
		At%	Wt%
C	K	21.4	10.1
O	K	44.0	27.7
Fe	K	22.6	49.4
Si	K	2.4	2.6
Na	K	2.8	2.5
Mg	K	0.7	0.7
Al	K	5.3	5.7
Ca	K	0.8	1.3

The XRD patterns of hematite/SiO_2 composite (Fig 9) exhibit sharp and intense peaks, signifying a high degree of crystallinity and confirming the primary phase of hematite [70]. These characteristic peaks align with the hematite database (ICDD No. 01-079-1741).

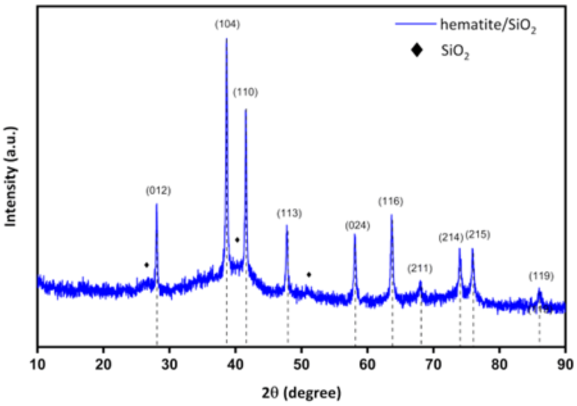

Figure 9. XRD Pattern of hematite/SiO$_2$ composite.

Notably, the strongest peaks, at the (1 0 4) and (1 1 0) lattice indices, match those of hematite$_{CA}$ (Fig 7). The patterns also show a raised background between 2θ = 25° and 45°, indicating amorphous silica is present in the composite. The average crystallite size, calculated from all peaks using the Debye-Scherrer equation, was 39.50 nm. This is significantly larger than that of hematite$_{CA}$, suggesting strong interactions or structural changes occurred between hematite and silica during synthesis.

4. Conclusion

This study successfully synthesized hematite using two different additives, citric acid and sodium hydroxide. Hematite$_{CA}$, synthesized with citric acid, yielded brownish-purple particles with a smaller crystallite size (13.58 nm) and higher crystallinity compared to hematite$_{SH}$. XRF characterization also confirmed the higher purity of hematite$_{CA}$ than hematite$_{SH.}$ Based on these results, hematite$_{CA}$ was selected for composite formation with purified silica. The addition of amorphous silica to hematite$_{CA}$ shifted the powder color to wine-red and introduced porous-like features.

Author contributions

Shirly Harissyah Alfiani: Investigation, Formal analysis, Writing-original draft, Visualization. **Qori'atun Ni'mah Salsabila**: Investigation, Writing-Review and Editing. **Reinardo Ramawijaya Kusuma**: Visualization, Formal Analysis. **Rifqi Almusawi Rafsanjani**: Conceptualization, Methodology, Software, Formal Analysis. **Habib Muhammad Zapar**: Conceptualization, Software, Validation. **Bagaskoro Pranata Ardhi**: Methodology, Resources. **Agus Purwanto**: Supervision, Project Administration, Funding Acquisition.

Conflicts of interest

The authors declare no conflicts of interest regarding the publication of this research.

Acknowledgement

The authors would like to acknowledge the support given by the PT. Cipta Mikro Material (CMiM) for providing the material, laboratories, and characterization facilities for this work.

References

[1] S.N. Zahra, F. Wulandari, M.R. Rauf, A. Ayuningsih, Methylene Blue Photodegradation Using Cu-decorated Cu2O Prepared by a Facile Electrochemical Deposition Method, *Chem. Mater.* **3** (2024) 71–79. https://doi.org/10.56425/cma.v3i3.81.

[2] R. Mulmeyda, R.R. Widakusuma, S.P. Chaerani, A. Purwanto, A. Rafsanjani, H.M. Zapar, B.P. Ardhi, Synthesis of α-Fe2O3 and α-Fe2 O3/SiO2 Composite from Geothermal Waste by Sol-Gel Method and Their Characterization, *Chem. Mater.* **4** (2025) 24–33.

[3] A. Ali, H. Zafar, M. Zia, I. ul Haq, A.R. Phull, J.S. Ali, A. Hussain, Synthesis, characterization, applications, and challenges of iron oxide nanoparticles, *Nanotechnol. Sci. Appl.* **9** (2016) 49–67. https://doi.org/10.2147/NSA.S99986.

[4] S. Bagheri, C.K. G, S. Bee Abd Hamid, Generation of Hematite Nanoparticles via Sol-Gel Method, 2013.

[5] F. Kraushofer, Z. Jakub, M. Bichler, J. Hulva, P. Drmota, M. Weinold, M. Schmid, M. Setvin, U. Diebold, P. Blaha, G.S. Parkinson, Atomic-Scale Structure of the Hematite α-Fe2O3(11-02) "R-Cut" Surface, *J. Phys. Chem.* **122** (2018) 1657–1669. https://doi.org/10.1021/acs.jpcc.7b10515.

[6] M.K. Ahmed, M.A. Zayed, S.I. El-dek, M.A. Hady, D.H. El Sherbiny, V. Uskoković, Nanofibrous ε-polycaprolactone scaffolds containing Ag-doped magnetite nanoparticles: Physicochemical characterization and biological testing for wound dressing applications in vitro and in vivo, *Bioact. Mater.* **6** (2021) 2070–2088. https://doi.org/10.1016/j.bioactmat.2020.12.026.

[7] N. Malhotra, J.-S. Lee, R.A.D. Liman, J.M.S. Ruallo, O.B. Villaflores, T.-R. Ger, C.-D. Hsiao, Potential Toxicity of Iron Oxide Magnetic Nanoparticles: A Review, *Molecules*. **25** (2020) 3159. https://doi.org/10.3390/molecules25143159.

[8] S. Saif, A. Tahir, Y. Chen, Green Synthesis of Iron Nanoparticles and Their Environmental Applications and Implications, *Nanomaterials*. **6** (2016) 209. https://doi.org/10.3390/nano6110209.

[9] I. Gritli, A. Bardaoui, J. Ben Naceur, S. Ammar, M. Abu Haija, S.M.A.S. Keshk, R. Chtourou, A facile approach for the synthesis of porous hematite and magnetite nanoparticles through sol-gel self-combustion, *Turkish*

J. Chem. **45** (2021) 1916–1932. https://doi.org/10.3906/kim-2104-59.

[10] L. Miftahul Khoiroh, D. Mardiana, A. Sabarudin, B. Ismuyanto, Synthesis of Hematite Pigments (α-Fe2O3) by Thermal Transformations of FeOOH, *J. Pure Appl. Chem. Res.* **2** (2013) 27–34. https://doi.org/10.21776/ub.jpacr.2013.002.01.120.

[11] N. Nurdini, M.M. Ilmi, E. Maryanti, P. Setiawan, G.T.M. Kadja, Ismunandar, Thermally-induced color transformation of hematite: insight into the prehistoric natural pigment preparation, *Heliyon*. **8** (2022) e10377. https://doi.org/10.1016/j.heliyon.2022.e10377.

[12] M. Hjiri, S. Algessair, R. Dhahri, A. Mirzaei, G. Neri, Gas sensing properties of hematite nanoparticles synthesized via different techniques, *RSC Adv.* **14** (2024) 17526–17534. https://doi.org/10.1039/d4ra02338b.

[13] Y. Li, J. Dang, Y. Ma, H. Ma, Hematite: A Good Catalyst for the Thermal Decomposition of Energetic Materials and the Application in Nano-Thermite, *Molecules*. **28** (2023). https://doi.org/10.3390/molecules28052035.

[14] L. Chun, X. Wu, X. Lou, Y. Zhang, Hematite nanoflakes as anode electrode materials for rechargeable lithium-ion batteries, *Electrochim. Acta*. **55** (2010) 3089–3092. https://doi.org/10.1016/j.electacta.2010.01.016.

[15] J. Hua, J. Gengsheng, Hydrothermal synthesis and characterization of monodisperse α-Fe2O3 nanoparticles, *Mater. Lett.* **63** (2009) 2725–2727. https://doi.org/10.1016/j.matlet.2009.09.054.

[16] Y. Xue, Y. Wang, A review of the α-Fe2O3 (hematite) nanotube structure: recent advances in synthesis, characterization, and applications, *Nanoscale*. **12** (2020) 10912–10932. https://doi.org/10.1039/d0nr02705g.

[17] S. Zeng, K. Tang, T. Li, Z. Liang, Hematite with the urchinlike structure: Its shape-selective synthesis, magnetism, and enhanced photocatalytic performance after TIO2 encapsulation, *J. Phys. Chem. C.* **114** (2010) 274–283. https://doi.org/10.1021/jp909111j.

[18] X. Su, C. Yu, C. Qiang, Synthesis of α-Fe2O 3 nanobelts and nanoflakes by thermal oxidation and study to their magnetic properties, *Appl. Surf. Sci.* **257** (2011) 9014–9018. https://doi.org/10.1016/j.apsusc.2011.05.091.

[19] S. Lian, E. Wang, Z. Kang, Y. Bai, L. Gao, M. Jiang, C. Hu, L. Xu, Synthesis of magnetite nanorods and porous hematite nanorods, *Solid State Commun.* **129** (2004) 485–490. https://doi.org/10.1016/j.ssc.2003.11.043.

[20] D. Hoffelner, M. Kundt, A.M. Schmidt, E. Kentzinger, P. Bender, S. Disch, Directing the orientational alignment of anisotropic magnetic nanoparticles using dynamic magnetic fields, *Faraday Discuss.* **181** (2015) 449–461. https://doi.org/10.1039/c4fd00242c.

[21] H. Wang, X. He, Y. Wang, Synthesis and characterization of flower-like hematite nanostructures, *Adv. Mater. Res.* **287–290** (2011) 169–172. https://doi.org/10.4028/www.scientific.net/AMR.287-290.169.

[22] C.J. Jia, L.D. Sun, F. Luo, X.D. Han, L.J. Heyderman, Z.G. Yan, C.H. Yan, K. Zheng, Z. Zhang, M. Takano, N. Hayashi, M. Eltschka, M. Kläui, U. Rüdiger, T. Kasama, L. Cervera-Gontard, R.E. Dunin-Borkowski, G. Tzvetkov, J. Raabe, Large-scale synthesis of single-crystalline iron oxide magnetic nanorings, *J. Am. Chem. Soc.* **130** (2008) 16968–16977. https://doi.org/10.1021/ja805152t.

[23] J.M. Meijer, L. Rossi, Preparation, properties, and applications of magnetic hematite microparticles, *Soft Matter*. **17** (2021) 2354–2368. https://doi.org/10.1039/d0sm01977a.

[24] W. Matysiak, T. Tański, M. Zaborowska, Electrospinning process and characterization of PVP/hematite nanofibers, *IOP Conf. Ser. Mater. Sci. Eng.* **461** (2018). https://doi.org/10.1088/1757-899X/461/1/012050.

[25] C. Gong, D. Chen, X. Jiao, Q. Wang, Continuous hollow α-Fe2O3 and α-Fe fibers prepared by the sol-gel method, *J. Mater. Chem.* **12** (2002) 1844–1847. https://doi.org/10.1039/b201243j.

[26] L. Chen, J. Li, Y. Lin, X. Liu, L. Lin, D. Li, Surface modification and characterization of γ-Fe2O 3 nanoparticles synthesized by chemically-induced transition, *Mater. Chem. Phys.* **141** (2013) 828–834. https://doi.org/10.1016/j.matchemphys.2013.06.011

[27] C. Yilmaz, U. Unal, Morphology and crystal structure control of α-Fe2O3 films by hydrothermal-electrochemical deposition in the presence of Ce3+ and/or acetate, F- ions, *RSC Adv.* **6** (2016) 8517–8527. https://doi.org/10.1039/c5ra20105e.

[28] M. Bai, W. Li, H. Yang, W. Dong, Q. Wang, Q. Chang, Morphology-controlled synthesis of MoS2 using citric acid as a complexing agent and self-assembly inducer for high electrochemical performance, *RSC Adv.* **12** (2022) 28463–28472. https://doi.org/10.1039/d2ra05351a.

[29] H. Liu, Y. Wei, P. Li, Y. Zhang, Y. Sun, Catalytic synthesis of nanosized hematite particles in solution, *Mater. Chem. Phys.* **102** (2007) 1–6. https://doi.org/10.1016/j.matchemphys.2006.10.001

[30] S. Lubis, I. Mustafa, Y. Ermanda, M. Ramadhani, Preparation of SiO_2/α-Fe_2O_3 Composite from Rice

Husk and Iron Sand as a Photocatalyst for Degradation of Acid Black 1 Dye, *J. Phys. Conf. Ser.* **1819** (2021) 012010. https://doi.org/10.1088/1742-6596/1819/1/012010.

[31] P.S. Shinde, P.S. Suryawanshi, K.K. Patil, V.M. Belekar, S.A. Sankpal, S.D. Delekar, S.A. Jadhav, A brief overview of recent progress in porous silica as catalyst supports, *J. Compos. Sci.* **5** (2021) 1–17. https://doi.org/10.3390/jcs5030075.

[32] R.K. Kankala, Y.H. Han, J. Na, C.H. Lee, Z. Sun, S. Bin Wang, T. Kimura, Y.S. Ok, Y. Yamauchi, A.Z. Chen, K.C.W. Wu, Nanoarchitectured Structure and Surface Biofunctionality of Mesoporous Silica Nanoparticles, *Adv. Mater.* **32** (2020). https://doi.org/10.1002/adma.201907035.

[33] S. Lubis, I. Mustafa, Y. Ermanda, M. Ramadhani, Preparation of SiO2/a-Fe2O3Composite from Rice Husk and Iron Sand as a Photocatalyst for Degradation of Acid Black 1 Dye, *J. Phys. Conf. Ser.* **1819** (2021). https://doi.org/10.1088/1742-6596/1819/1/012010.

[34] Q. Dong, N. Kumada, Y. Yonesaki, T. Takei, N. Kinomura, D. Wang, Template-free hydrothermal synthesis of hollow hematite microspheres, *J. Mater. Sci.* **45** (2010) 5685–5691. https://doi.org/10.1007/s10853-010-4634-x.

[35] C. Park, J. Jung, C.W. Lee, J. Cho, Synthesis of Mesoporous α-Fe 2O3 Nanoparticles by Non-ionic Soft Template and Their Applications to Heavy Oil Upgrading, *Sci. Rep.* **6** (2016) 1–9. https://doi.org/10.1038/srep39136.

[36] E. Delahaye, V. Escax, N. El Hassan, A. Davidson, R. Aquino, V. Dupuis, R. Perzynski, Y.L. Raikher, "Nanocasting": using SBA-15 silicas as hard templates to obtain ultrasmall monodispersed γ-Fe2O3 nanoparticles, *J. Phys. Chem. B*. **110** (2006) 26001–26011. https://doi.org/10.1021/jp0647075.

[37] S. Fatimah, R. Ragadhita, D. Fitria, A. Husaeni, A. Bayu, D. Nandiyanto, How to calculate crystallite size from X-ray diffraction (XRD) using Scherrer method, **2** (2022) 65–76.

[38] D. Bokov, A. Turki Jalil, S. Chupradit, W. Suksatan, M. Javed Ansari, I.H. Shewael, G.H. Valiev, E. Kianfar, Nanomaterial by Sol-Gel Method: Synthesis and Application, *Adv. Mater. Sci. Eng.* **2021** (2021) 1–21. https://doi.org/10.1155/2021/5102014.

[39] M. Elma, A. Paramita, A. Sumardi, Pengaruh Penambahan Dual Katalis Pada Silica-Carbon Xerogel Sebagai Material Pelapis Organo Silica Membranes, *Konversi*. **7** (2018) 55–61. https://doi.org/10.20527/k.v7i2.6498.

[40] R.K. Nagarale, G.S. Gohil, V.K. Shahi, Recent developments on ion-exchange membranes and electro-membrane processes, *Adv. Colloid Interface Sci.* **119** (2006) 97–130. https://doi.org/10.1016/j.cis.2005.09.005.

[41] L. Novita, I. Idris, Effectiveness of silica gel from palm kernel shell ash as a moisture absorber of bottle packaging medicine, *IOP Conf. Ser. Earth Environ. Sci.* **1041** (2022) 1–7. https://doi.org/10.1088/1755-1315/1041/1/012044.

[42] A. Daulay, Andriayani, Marpongahtun, S. Gea, Extraction silica from rice husk with naoh leaching agent with temperature variation burning rice husk, *Rasayan J. Chem.* **14** (2021) 2125–2128. https://doi.org/10.31788/RJC.2021.1436351.

[43] S. Silviana, G.J. Sanyoto, A. Darmawan, H. Sutanto, Geothermal silica waste as sustainable amorphous silica source for the synthesis of silica xerogels, *Rasayan J. Chem.* **13** (2020) 1692–1700. https://doi.org/10.31788/RJC.2020.1335701.

[44] S. Affandi, H. Setyawan, S. Winardi, A. Purwanto, R. Balgis, A facile method for production of high-purity silica xerogels from bagasse ash, *Adv. Powder Technol.* **20** (2009) 468–472. https://doi.org/10.1016/j.apt.2009.03.008.

[45] Q. Cai, J. Jiang, B. Ma, Z. Shao, Y. Hu, B. Qian, L. Wang, Efficient removal of phosphate impurities in waste phosphogypsum for the production of cement, *Sci. Total Environ.* **780** (2021) 146600. https://doi.org/10.1016/j.scitotenv.2021.146600.

[46] E. Vranic, Amorphous Pharmaceutical Solids, *Bosn. J. Basic Med. Sci.* **4** (2004) 35–39. https://doi.org/10.1016/j.addr.2016.04.011.

[47] P.S. Utama, R. Yamsaensung, C. Sangwichien, Silica gel derived from palm oil mill fly ash, *Songklanakarin J. Sci. Technol.* **40** (2018) 121–126. https://doi.org/10.14456/sjst-psu.2018.27.

[48] H. Hamdan, M.N.M. Muhid, S. Endud, E. Listiorini, Z. Ramli, 29Si MAS NMR, XRD and FESEM studies of rice husk silica for the synthesis of zeolites, *J. Non. Cryst. Solids*. **211** (1997) 126–131. https://doi.org/10.1016/S0022-3093(96)00611-4.

[49] R.K. Biswas, P. Khan, S. Mukherjee, A.K. Mukhopadhyay, J. Ghosh, K. Muraleedharan, Study of short range structure of amorphous Silica from PDF using Ag radiation in laboratory XRD system, RAMAN and NEXAFS, *J. Non. Cryst. Solids*. **488** (2018) 1–9. https://doi.org/10.1016/j.jnoncrysol.2018.02.037.

[50] D.M. González-García, L. Téllez-Jurado, F.J. Jiménez-Álvarez, L. Zarazua-Villalobos, H. Balmori-Ramírez, Evolution of a natural pozzolan-based geopolymer alkalized in the presence of sodium or potassium silicate/hydroxide solution, *Constr. Build. Mater.* **321** (2022) 126305.

https://doi.org/10.1016/j.conbuildmat.2021.126305.

[51] Z. Rahimabady, M.M. Bagheri – Mohagheghi, A. Shirpay, SiO2@NiO core/ shell nanoparticles as high-performance anode materials: Synthesis and characterizations of structural, optical and magnetic properties, *Surfaces and Interfaces*. **29** (2022) 101801. https://doi.org/10.1016/j.surfin.2022.101801.

[52] H. Ismail, Z. Zainuddin, H. Mohamad, M.A.A. Hamid, Compatibility of Concentrated NaOH as a Precipitation Agent in the Synthesis of Maghemite (γ-Fe2O3) Nanoparticles via Co-precipitation Method, *J. Phys. Sci.* **33** (2022) 61–75. https://doi.org/10.21315/jps2022.33.2.4.

[53] L. Zhao, F. Di, D. Wang, L. Hong Guo, Y. Yang, B. Wan, H. Zhang, Chemiluminescence of carbon d dots und er strong alkaline solutions: A novel in sight into carbon dots optical properties, *Nanoscale*. **5** (2013) 2655–2658. https://doi.org/10.1039//b000000x.

[54] X. Zhang, L. Chen, R. Liu, D. Li, X. Ge, G. Ge, The role of the OH group in citric acid in the coordination with Fe3O4 nanoparticles, *Langmuir*. **35** (2019) 8325–8332. https://doi.org/10.1021/acs.langmuir.9b00208.

[55] M. Parashar, V.K. Shukla, R. Singh, Metal oxides nanoparticles via sol–gel method: a review on synthesis, characterization and applications, *J. Mater. Sci. Mater. Electron.* **31** (2020) 3729–3749. https://doi.org/10.1007/s10854-020-02994-8.

[56] N. Utari, H. Maulidina, R. Arilasita, H. Widiyandari, Suharno, B. Purnama, Citric acid concentration tune of structural and magnetic properties in hematite (α−Fe2O3) nanoparticles synthesized by sol−gel method, *Mater. Res. Express*. **10** (2023). https://doi.org/10.1088/2053-1591/acbf0c.

[57] P.E. Pergola, S. Fishbane, T. Ganz, Novel Oral Iron Therapies for Iron Deficiency Anemia in Chronic Kidney Disease, *Adv. Chronic Kidney Dis.* **26** (2019) 272–291. https://doi.org/10.1053/j.ackd.2019.05.002.

[58] K. Zanotti, K. Igal, M.B. Colombo Migliorero, V. Gomes Zuin, P.G. Vázquez, Synthesis of Silica-Based Materials Using Bio-Residues through the Sol-Gel Technique, *Sustain. Chem.* **2** (2021) 670–685. https://doi.org/10.3390/suschem2040037.

[59] P. Liang, W. Yang, H. Peng, S. Zhao, Efficient Degradation of Methylene Blue in Industrial Wastewater and High Cycling Stability of Nano ZnO, **29** (2024) 5584. https://doi.org/10.3390/molecules29235584.

[60] M. Siampiringue, C. Massard, E. Caudron, Y. Sibaud, M. Sarakha, K.O. Awitor, Impact of Annealing Treatment on the Behaviour of Titanium Dioxide Nanotube Layers, *J. Biomater. Nanobiotechnol.* **07** (2016) 142–153. https://doi.org/10.4236/jbnb.2016.73015.

[61] E. Castagnotto, F. Locardi, S. Slimani, D. Peddis, L. Gaggero, M. Ferretti, Characterization of the Caput Mortuum purple hematite pigment and synthesis of a modern analogue, *Dye. Pigment.* **185** (2021) 108881. https://doi.org/10.1016/j.dyepig.2020.108881.

[62] A. Fatmaliana, M. Maulinda, N. Sari, Synthesis and characterization of hematite (Fe_2O_3) from iron ore and magnetite (Fe_3O_4) from iron sand through the precipitation method for industrial raw materials, *J. Neutrino J. Fis. Dan Apl.* **12** (2020) 37–42. https://doi.org/10.18860/neu.v12i2.8183.

[63] M.A. Marjeghal, A. Sedghi, S. Baghshahi, The effect of the citric acid to metal nitrates molar ratio on the structural and magnetic properties of strontium hexaferrite nanoparticles synthesized by the sol-gel combustion method, *J. Alloys Compd.* **968** (2023) 171765. https://doi.org/10.1016/j.jallcom.2023.171765.

[64] D. Bikiaris, S. Daniilia, S. Sotiropoulou, O. Katsimbiri, E. Pavlidou, A.P. Moutsatsou, Y. Chryssoulakis, Ochre-differentiation through micro-Raman and micro-FTIR spectroscopies: Application on wall paintings at Meteora and Mount Athos, Greece, *Spectrochim. Acta - Part A Mol. Biomol. Spectrosc.* **56** (2000) 3–18. https://doi.org/10.1016/S1386-1425(99)00134-1.

[65] F. Davar, H. Hadadzadeh, T.S. Alaedini, Single-phase hematite nanoparticles: Non-alkoxide sol–gel based preparation, modification and characterization, *Ceram. Int.* **42** (2016) 19336–19342. https://doi.org/10.1016/j.ceramint.2016.09.104.

[66] R.A. Kerner, E.D. Christensen, S.P. Harvey, J. Messinger, S.N. Habisreutinger, F. Zhang, G.E. Eperon, L.T. Schelhas, K. Zhu, J.J. Berry, D.T. Moore, Analytical Evaluation of Lead Iodide Precursor Impurities Affecting Halide Perovskite Device Performance, *ACS Appl. Energy Mater.* **6** (2023) 295–301. https://doi.org/10.1021/acsaem.2c02842.

[67] A. Roy, C.P. Healey, N.E. Larm, P. Ishtaweera, M. Roca, G.A. Baker, The Huge Role of Tiny Impurities in Nanoscale Synthesis, *ACS Nanosci. Au*. **4** (2024) 176–193. https://doi.org/10.1021/acsnanoscienceau.3c00056.

[68] R.M. Cornell, U. Schwertmann, Influence of Organic Anions on the Crystallization of Ferrihydrite, *Clays Clay Miner.* **27** (1979) 402–410. https://doi.org/10.1346/ccmn.1979.0270602.

[69] X. Pan, X. Su, S. Hua, Y. Wei, Z. Feng, Y. Zhao, W. Huang, Activated carbon as a catalyst to promote the reactivity of hydroquinone in skin whitening cosmetics, *J. Porous Mater.* (2024). https://doi.org/10.1007/s10934-024-01720-7.

[70] Q.N. Salsabila, F.G. Kenaya, M.F. Aulia, M. Athariq, Additive-free Electrodeposition of SnCoNi Trimetallic Catalysts for Ethanol Electrooxidation, *Chem. Mater.* **3** (2024) 90–97. https://doi.org/10.56425/cma.v3i3.84.